ADVANCED MATERIALS
www.advmat.de

A Cu_3BHT-Graphene van der Waals Heterostructure with Strong Interlayer Coupling for Highly Efficient Photoinduced Charge Separation

Zhiyong Wang, Shuai Fu, Wenjie Zhang, Baokun Liang, Tsai-Jung Liu, Mike Hambsch, Jonas F. Pöhls, Yufeng Wu, Jianjun Zhang, Tianshu Lan, Xiaodong Li, Haoyuan Qi, Miroslav Polozij, Stefan C. B. Mannsfeld, Ute Kaiser, Mischa Bonn, R. Thomas Weitz, Thomas Heine, Stuart S. P. Parkin, Hai I. Wang,* Renhao Dong,* and Xinliang Feng**

Two-dimensional van der Waals heterostructures (2D vdWhs) are of significant interest due to their intriguing physical properties critically defined by the constituent monolayers and their interlayer coupling. Synthetic access to 2D vdWhs based on chemically tunable monolayer organic 2D materials remains challenging. Herein, the fabrication of a novel organic–inorganic bilayer vdWh by combining π-conjugated 2D coordination polymer (2DCP, i.e., Cu_3BHT, BHT = benzenehexathiol) with graphene is reported. Monolayer Cu_3BHT with detectable μm^2-scale uniformity and atomic flatness is synthesized using on-water surface chemistry. A combination of diffraction and imaging techniques enables the determination of the crystal structure of monolayer Cu_3BHT with atomic precision. Leveraging the strong interlayer coupling, Cu_3BHT-graphene vdWh exhibits highly efficient photoinduced interlayer charge separation with a net electron transfer efficiency of up to 34% from Cu_3BHT to graphene, superior to those of reported bilayer 2D vdWhs and molecular-graphene vdWhs. This study unveils the potential for developing novel 2DCP-based vdWhs with intriguing physical properties.

1. Introduction

Two-dimensional van der Waals heterostructures (2D vdWhs) constitute a new class of artificial materials constructed by vertically stacking atomically thin 2D crystals, including graphene, transition metal dichalcogenides (TMDs), and hexagonal boron nitride (*h*-BN), which are held together by vdW interactions.[1] The lack of direct chemical bonding in vdWhs affords complete freedom in selecting 2D materials, unrestricted by constraints of crystal symmetry, structure, and lattice matching.[2] Thanks to their atomically thin nature, the properties of vdWhs can be tailored by not only individual constituents but also interlayer coupling, giving rise to new quantum states and phenomena.[3] These unique characteristics have established vdWhs as a versatile platform for a

Z. Wang, W. Zhang, Y. Wu, T. Lan, X. Li, S. S. P. Parkin, X. Feng
Department of Synthetic Materials and Functional Devices
Max Planck Institute of Microstructure Physics
06120 Halle (Saale), Germany
E-mail: stuart.parkin@mpi-halle.mpg.de; xinliang.feng@tu-dresden.de

Z. Wang, S. Fu, T.-J. Liu, J. Zhang, X. Li, M. Polozij, T. Heine, R. Dong, X. Feng
Center for Advancing Electronics Dresden (cfaed) and Faculty of Chemistry and Food Chemistry
Technische Universität Dresden
01062 Dresden, Germany
E-mail: renhaodong@sdu.edu.cn

S. Fu, M. Bonn, H. I. Wang
Department of Molecular Spectroscopy
Max Planck Institute for Polymer Research
55128 Mainz, Germany
E-mail: h.wang5@uu.nl

The ORCID identification number(s) for the author(s) of this article can be found under https://doi.org/10.1002/adma.202311454

DOI: 10.1002/adma.202311454

B. Liang, H. Qi, U. Kaiser
Central Facility for Electron Microscopy
Electron Microscopy of Materials Science
Ulm University
89081 Ulm, Germany

M. Hambsch, S. C. B. Mannsfeld
Center for Advancing Electronics Dresden (cfaed) and Faculty of Electrical and Computer Engineering
Technische Universität Dresden
01069 Dresden, Germany

J. F. Pöhls, R. T. Weitz
First Institute of Physics
Georg August University of Göttingen
37077 Göttingen, Germany

M. Polozij, T. Heine
Helmholtz-Zentrum Dresden-Rossendorf
Institute of Resource Ecology
04318 Leipzig, Germany

T. Heine
Department of Chemistry
Yonsei University
120-749 Seoul, Republic of Korea

wide spectrum of applications, including tunneling transistors,[4] photodetectors,[5] and light-emitting devices,[6] with unprecedented functionalities. While vdWhs hold great promise for developing new materials and device concepts, the thus-far reported 2D vdWhs are mainly based on the assembly of monolayer inorganic 2D crystals. Exploring novel 2D vdWhs based on monolayer organic 2D materials, characterized by customizable structures and properties,[7] is of significance but remains rarely explored. This is primarily because of the difficulty in synthesizing organic 2D materials by controlling reactions at the monolayer scale while maintaining large-area uniformity and atomic flatness. Moreover, the limited availability of techniques presents significant challenges in characterizing atomically thin organic 2D layers, due to their high electron beam and X-ray sensitivity.[8]

In this study, we report the first example of novel organic-inorganic bilayer vdWh based on π-d conjugated 2D coordination polymer (2DCP, i.e., Cu_3BHT (BHT = benzenehexathiol), also known as 2D conjugated metal-organic framework (2D c-MOF)). Monolayer Cu_3BHT with strong π-d conjugation and planar structure in the 2D plane is first synthesized on the water surface, presenting as a polycrystalline film exhibiting considerable uniformity and atomic flatness. The crystal structure is resolved by using in situ grazing-incidence wide-angle X-ray diffraction (GIXD) and high-resolution transmission electron microscopy (HRTEM) imaging, elucidating the Kagome lattice with atomic precision (resolution, ≈1.2 Å). We show that vertically stacking monolayer Cu_3BHT and graphene through a wet transfer technique enables the creation of cm^2-scale Cu_3BHT-graphene vdWhs with intimate and uniform contacts. Raman and terahertz time-domain spectroscopy (THz-TDS) studies, combined with electrical measurements and theoretical modeling, demonstrate significant hole transfer from monolayer Cu_3BHT to graphene (hence downshift of the Fermi level (E_F) in graphene) upon contact due to strong interlayer electronic coupling. Furthermore, time-resolved THz spectroscopy (TRTS) reveals highly efficient photoinduced net electron gain in graphene (up to 34%), superior to those of graphene-based bilayer inorganic/organic vdWhs (up to 10%).[9] These findings unveil the possibilities for exploring novel 2D c-MOF-based vdWhs with manipulable orbital distribution, interfacial band alignment, and interlayer coupling.

2. Results

Monolayer Cu_3BHT was synthesized for the first time using the on-water surface chemistry, as schematically illustrated in **Figure** 1a,b. The synthetic procedure involved three steps: in Step 1, 50 µL of BHT solution (0.3 mg mL^{-1}) in chloroform/dimethylformamide (2:1, v/v) was spread on the water surface, followed by compressing the surface with a pair of Delrin barriers. To evaluate the pre-organization behavior of BHT on the water surface, the surface pressure-mean molecular area (π-A) isotherm was recorded. As shown in Figure S1, Supporting Information, the π-A isotherm shows a sharp increase in surface pressure upon compression when A reaches ≈9.5 $Å^2$, indicating that the BHT molecules undergo phase transitions from the gas phase into the crystalline phase. Consistency between the measured A values and the theoretical area of BHT (≈10 $Å^2$) manifests the formation of close-packed BHT molecules lying flat on the water surface. In Step 2, 5 mL $Cu(NO_3)_2$ aqueous solution (1 mg mL^{-1}) was injected into the water subphase to initiate the 2D coordination polymerization between Cu^{2+} and BHT ligands by forming Cu—S bonds on the water surface. After leveraging the polymerization for 5 h (Step 3), the Cu_3BHT film with a large lateral size of ≈50 cm^2 was obtained on the water surface and then transferred horizontally onto different substrates for various characterizations.

As shown in Figure 1c and Figure S2, Supporting Information, the as-synthetic Cu_3BHT film displays a detectable $µm^2$-scale uniformity with a monolayer thickness of ≈0.8 nm and a root mean square (RMS) roughness of 0.1 nm over an area of 10 × 10 $µm^2$. We attribute the realization of atomically flat films to the inherently planar structure of Cu_3BHT within the 2D conjugated plane, which guarantees strong interlayer coupling with graphene upon the assembly of vdWhs. Surface-enhanced Raman spectra of monolayer Cu_3BHT show the disappearance of the -SH peak at 2512 cm^{-1}, indicating efficient coordination between Cu and SH groups (Figure S3, Supporting Information). UV/vis absorption spectra of Cu_3BHT with different layer numbers reveal a linear relationship between the absorbance value at 270 nm and the number of layers, following the Beer–Lambert law (Figure S4, Supporting Information). The Tauc plot indicates a direct bandgap of ≈0.38 eV for monolayer Cu_3BHT (Figure S5, Supporting Information). This observation aligns with the results obtained by ultraviolet photoelectron spectroscopy (UPS), where the work function and valence band maximum of monolayer Cu_3BHT are calculated to be −4.38 and −4.63 eV versus vacuum, respectively (Figure S6, Supporting Information). Furthermore, we conducted variable-temperature conductivity measurements, which illustrate an increase in electrical conductivity from 100 to 300 K (Figure S7, Supporting Information), supporting the semiconducting nature of monolayer Cu_3BHT.

To confirm the crystallinity of the obtained monolayer Cu_3BHT, we conducted grazing-incidence X-ray diffraction (GIXD) measurements on the water surface. As shown in Figure 1d, the GIXD pattern shows unambiguously three in-plane Bragg diffraction peaks at Q_{xy} = 0.87, 1.48, and 1.75 $Å^{-1}$, corresponding to the 100, 110, and 200 Bragg reflections of a hexagonal lattice (d-spacing, 0.72 nm). The optimized structure model of monolayer Cu_3BHT, obtained by density functional theory (DFT) calculations, supports well with the experimental observations. Unlike the high electron beam sensitivity of hydrogen-rich monolayer 2D polymers and 2DCPs,[7a,b,10] the absence of hydrogen in the Cu_3BHT framework offers high stability under electron radiation and thus the opportunity for further investigation of its crystal structure by aberration-corrected

H. I. Wang
Nanophotonics
Debye Institute for Nanomaterials Science
Utrecht University
Utrecht 3584 CC, the Netherlands
R. Dong
Key Laboratory of Colloid and Interface Chemistry of the Ministry of Education
School of Chemistry and Chemical Engineering
Shandong University
Jinan 250199, China

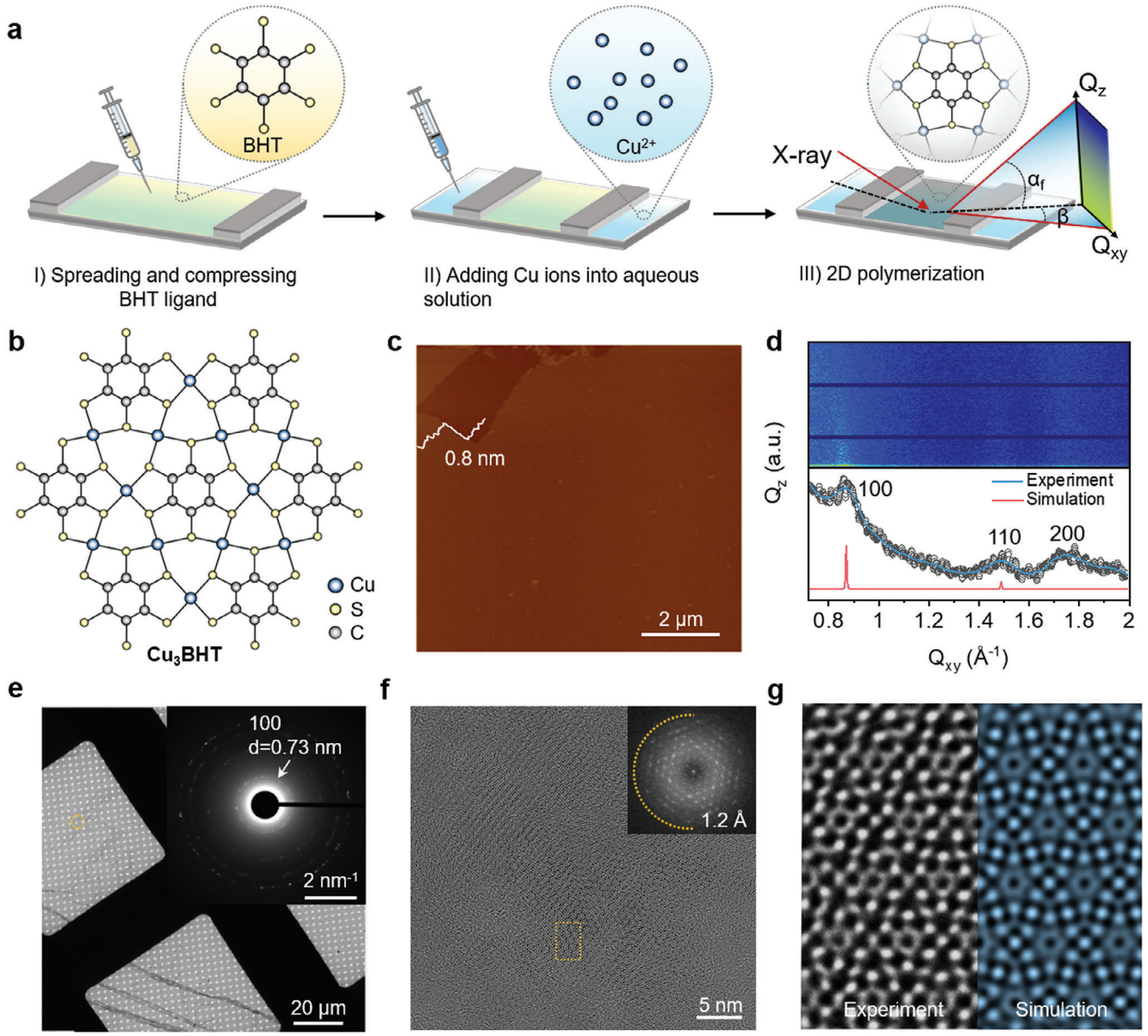

Figure 1. Synthesis and structural characterization of monolayer Cu_3BHT. a) Synthetic scheme of monolayer Cu_3BHT using the Langmuir–Blodgett method. b) Schematic structure of Cu_3BHT. Cu, C, and S atoms are shown in blue, grey, and yellow, respectively. c) AFM image and height profile of monolayer Cu_3BHT. d) GIXD pattern and in-plane (near $Q_z = 0$, Q represents the scattering vector) projection of the monolayer Cu_3BHT measured on the water surface. e) TEM image of monolayer Cu_3BHT. Inset: SAED pattern from the marked (yellow circle) region. f) AC-HRTEM image of Cu_3BHT denoised using Wiener filtering. Inset: corresponding FFT pattern. g) Left: the enlarged image of the highlighted area shown in (f). Right: simulated AC-HRTEM image of Cu_3BHT (thickness, monolayer; defocus, 6 nm).

high-resolution transmission electron microscopy (AC-HRTEM). As presented in Figure 1e, the sharp arcs in the selected area electron diffraction (SAED) pattern reveal the polycrystalline nature of Cu_3BHT. The nearest reflections at 1.37 nm^{-1} correspond to a real d-spacing of 0.73 nm, confirming the GIXD results. Notably, atomic resolution imaging of Cu_3BHT was achieved with a C_c/C_s-corrected SALVE instrument at 80 kV. As shown in Figure 1f, the AC-HRTEM image presents a highly ordered hexagonal unit cell with a lattice spacing of 0.73 nm, in agreement with the (100) plane of Cu_3BHT. The fast Fourier transform (FFT) image displays Bragg reflection spots to high spatial frequency, which is characteristic of good crystallinity and reveals an ordered lattice structure in the detectable area (tens of nm). In the enlarged AC-HRTEM image (Figure 1g), the structure of Cu_3BHT is visible at the atomic level (resolution, ≈1.2 Å), which agrees qualitatively with the simulated one (Figure 1g, inset) and the previously reported multilayer samples.[11]

We then fabricated the novel 2D vdWh by combining monolayer Cu_3BHT with large-area chemical vapor deposited (CVD) graphene using a wet transfer technique (**Figure 2**a, see Experimental Section). The resulting vdWh was then washed and

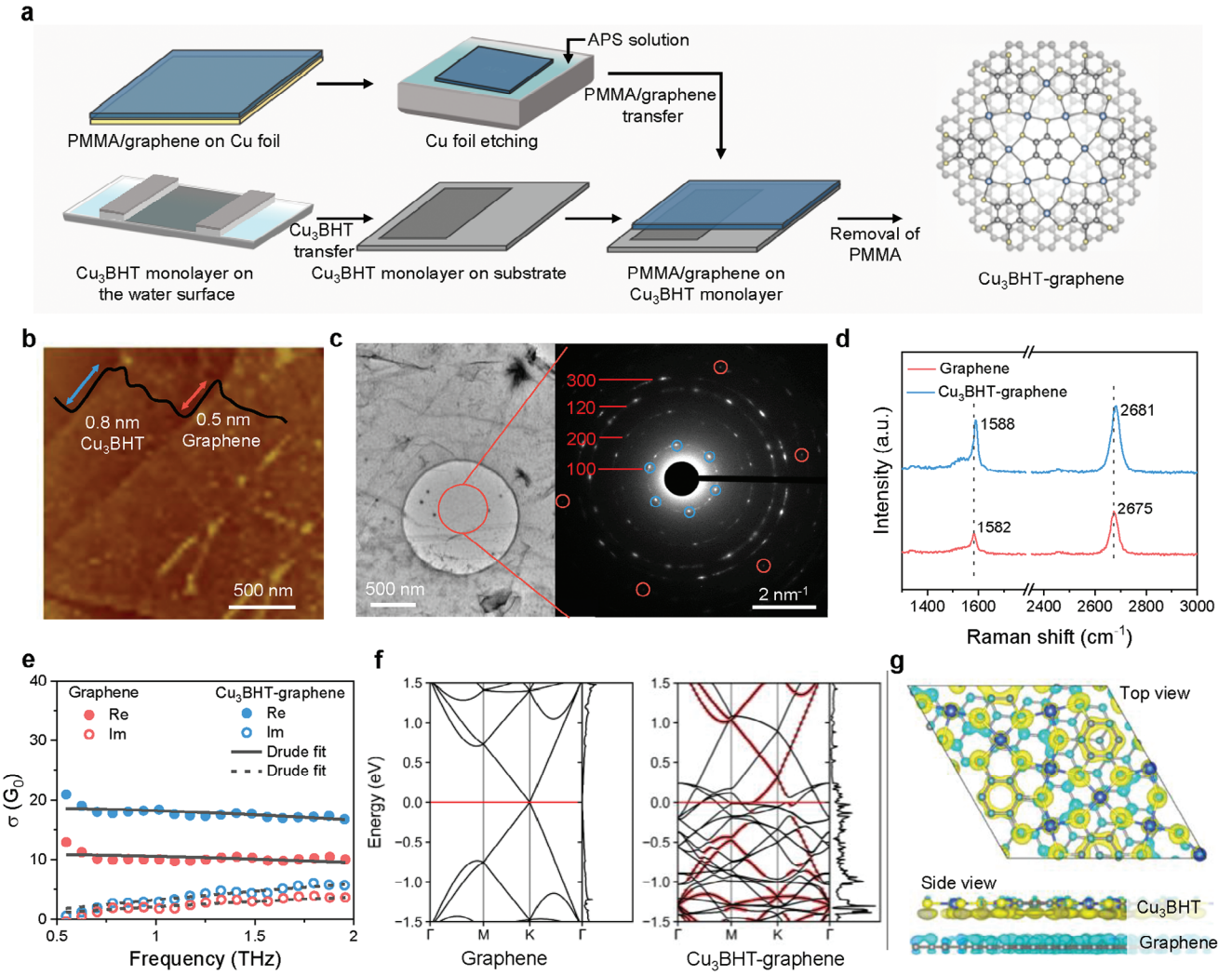

Figure 2. Morphological and interlayer coupling characterization of Cu_3BHT-graphene vdWh. a) Schematic of the preparation of Cu_3BHT-graphene vdWh by a wet transfer technique. b) AFM image and height profile of monolayer Cu_3BHT (blue line) and graphene (yellow line) in the vdWh. c) TEM image, and corresponding SAED pattern of Cu_3BHT-graphene vdWh with indexed diffraction spots. d) Raman spectra of graphene before and after deposition of monolayer Cu_3BHT. In the vdWh, the well-preserved symmetry of the G- and 2D-modes indicates that graphene maintains its structural integrity after contact with Cu_3BHT. e) Frequency-resolved complex sheet conductivity $\sigma_s(\omega)$ of bare graphene (red) and Cu_3BHT-graphene vdWh (blue) in units of quantum conductance $G_0 = 2e^2/h$. The solid and dashed lines correspond to the Drude fits of the real and imaginary parts of $\sigma_s(\omega)$, respectively. f) Band structures of graphene and graphene-Cu_3BHT vdWh with 3° twist angle and their corresponding densities of states (DOS). Red dots in the Cu_3BHT-graphene vdWh band structure indicate bands originating predominantly from the graphene layer. g) The CDD of Cu_3BHT-graphene vdWh. The charge density isosurfaces value is set to 0.0003 e $Bohr^{-3}$ with yellow and blue showing an increase and decrease of electron density, respectively.

annealed at 300 °C under an H_2-Ar atmosphere to remove poly(methyl methacrylate) (PMMA) and trapped interfacial contaminants, and to enhance the interaction between Cu_3BHT and graphene. Figure 2b and Figure S8, Supporting Information, show the morphology of Cu_3BHT-graphene vdWh, from which the monolayer nature of both Cu_3BHT and graphene layers was confirmed. We further characterized the structures of Cu_3BHT-graphene vdWh using SAED and TEM (Figure 2c, left). Importantly, the SAED pattern from the overlapping Cu_3BHT-graphene region shows two sets of diffraction spots (Figure 2c, right and Figure S9, Supporting Information), with the inner and outer sets corresponding to Cu_3BHT and graphene, respectively. Note that no clear Moiré superlattice structure was observed using AC-HRTEM imaging, mainly due to the polycrystalline nature of Cu_3BHT.[12]

We conducted Raman and THz measurements to study the unique electronic properties of this novel Cu_3BHT-graphene 2D vdWh. Raman spectra of graphene, taken before and after deposition of monolayer Cu_3BHT, were averaged from Raman mapping images (Figure S10, Supporting Information) and are presented in Figure 2d. Pristine graphene exhibits G- and 2D-modes at 1582 and ≈2675 cm^{-1}, respectively, indicative of high-quality monolayer graphene with negligible strain and doping effects.[13] The deposition of monolayer Cu_3BHT resulted in a blue-shift (≈6 cm^{-1}) of both G- (≈1588 cm^{-1}) and 2D (2681 cm^{-1})-modes, indicating an increased hole concentration in graphene.[13a] By

deconvoluting the contributions of strain and doping using the correlation between G-mode and 2D-mode,[13b] we find that monolayer Cu_3BHT coverage on graphene introduces negligible strain but substantial hole density modulation, whereby the E_F in graphene shifts downward by ≈0.29 eV in the vdWh (equivalent to a hole concentration of $\approx 5 \times 10^{12}$ cm^{-2}) (see Experimental Section).

To gain deeper insight into the ground-state charge transfer (CT) effect upon vdWh formation, we employ TRTS (see Experimental section) to investigate the frequency-resolved complex sheet conductivity $\sigma(\omega)$ of graphene with and without monolayer Cu_3BHT interactions. Figure S11, Supporting Information, compares THz waveforms transmitted through different sample regions. Monolayer Cu_3BHT was found to exhibit almost no THz absorption compared to the blank substrate, revealing its negligible intrinsic conductivity due to its semiconducting and polycrystalline nature (and, therefore, low carrier density). In contrast, both bare graphene and Cu_3BHT-graphene vdWh exhibit attenuated transmitted THz fields. Given the negligible intrinsic conductivity of monolayer Cu_3BHT, the observed THz absorption (and thus conductivity) in bare graphene and Cu_3BHT-graphene vdWh can be attributed to the presence of conductive charge carriers in the graphene layer. As shown in Figure 2e, $\sigma(\omega)$ of bare graphene and Cu_3BHT-graphene vdWh can be well described by the Drude model (Equation (1))[14]

$$\sigma(\omega) = \frac{D}{\pi\left(\frac{1}{\tau} - i\omega\right)} \tag{1}$$

where ω is the angular frequency, D is the Drude weight related to the carrier density N and E_F, and τ is the charge scattering time. The fits infer τ and E_F to be 31 ± 2 fs and ≈0.23 eV for bare graphene, and 29 ± 1 fs and ≈0.43 eV for monolayer Cu_3BHT-covered graphene. These findings indicate a downshift of E_F in graphene by ≈0.20 eV upon vdWh formation, corroborating the Raman results.

To further explore the electrical characteristics evolution upon vdWh formation, we calculated their band structures (Figure 2f and Figure S12, Supporting Information) and electrostatic potentials (Figure S13, Supporting Information) using DFT. The calculated E_F of the vdWh is positioned at 0.315 eV below the graphene Dirac cone, signifying a prominent hole accumulation in graphene. Figure S13a, Supporting Information, shows that the incorporation of monolayer Cu_3BHT elevates the work function (W_F) of graphene from 4.530 to 4.856 eV (vs vacuum level, see Supporting Information). Furthermore, we tested three different twist angles, all of which yielded consistent qualitative results, suggesting that the observed effect is independent of interlayer twist and, consequently, the domain position within the polycrystalline material (Figures S12 and S13, Supporting Information). The charge density difference (CDD) isosurfaces highlight a strong interlayer coupling between monolayer Cu_3BHT and graphene (Figure 2g), leading to electron accumulation in Cu_3BHT and hole accumulation in graphene. These results align with our Raman and TRTS observations and identify that the strong interlayer coupling contributes to significant hole transfer from monolayer Cu_3BHT to graphene upon contact. The interfacial charge equilibrium establishes a built-in electric field directed from graphene toward Cu_3BHT. We anticipate that the strong interlayer coupling originates from the following two factors: 1) intimate contact enabled by their atomically flat surfaces;[2,15] 2) dense wavefunction overlap at the interface contributed by highly delocalized electronic orbitals in Cu_3BHT[16] and massless Dirac Fermions in graphene.[17]

We further fabricated gated Hall bar devices to investigate the electronic properties of Cu_3BHT-graphene vdWh under external electric and magnetic fields (**Figure 3a**). As shown in Figure 3b, the conductance-gate voltage curve of graphene exhibits a distinct minimum at a gate voltage of ≈78 V, which corresponds to the Dirac point. The positive sign of V_D (i.e., p-doping of graphene) can be mainly attributed to the contact effect caused by oxygen dangling bonds in the SiO_2 substrate.[18] Furthermore, it has been reported that the adsorption of water/oxygen molecules or PMMA residues could also contribute to the p-doping effect.[19] In contrast, the Cu_3BHT-graphene vdWh displays a broader valley in the curve, positioned around a gate voltage of ≈117 V. This significant shift in the Dirac point suggests the transfer of holes from Cu_3BHT to the graphene layer,[20] requiring a higher gate voltage to raise the E_F to the Dirac point. Figure 3c shows the gate voltage-dependent Hall coefficients, which exhibit reversals of signs at the Dirac points due to the change from hole accumulation to electron accumulation. In pristine graphene, either holes or electrons dominate the Hall signals, leading to a sharp reversal. However, in Cu_3BHT-graphene vdWh, both holes and electrons contribute to the Hall signal, with their respective contributions varying as a function of gate voltage, resulting in a gradual reversal. We further investigate the magnetic field dependence of normalized longitudinal resistance R_{xx}/R_{xx_min}, as presented in Figure 3d and Figure S14, Supporting Information. These curves are interpolated by data points measured at the neighborhoods of their Dirac points. Close to zero field, a small peak is observed, which could be related to weak localization.[21] The remaining curves exhibit positive magneto-resistance, consistent with the Drude model. The full mapping of gate voltage-dependent magneto-resistance of graphene and Cu_3BHT-graphene vdWh is depicted in Figure 3e. In graphene, a 130% positive magneto-resistance is observed around the Dirac point, which diminishes significantly as the system moves away from the Dirac point, aligning with previous reports.[22] However, in Cu_3BHT-graphene vdWh, the magneto-resistance remains largely unchanged over a wide range of gate voltages.

To elucidate the light-induced interfacial charge carrier separation and recombination in Cu_3BHT-graphene vdWhs, we measured photoconductivity ($\Delta\sigma$) dynamics using TRTS.[23] **Figure 4a,b** shows that following photoexcitation by a 1.55 eV ultrashort pulsed laser, bare graphene experiences a reduction in conductivity. This so-called "negative $\Delta\sigma$" has been widely reported in metallic systems including doped graphene,[24] due to the enhanced momentum scattering experienced by photogenerated hot carriers. The electronic system relaxes back to equilibrium on the sub-10 ps time scale following hot carrier cooling in bare graphene. Conversely, in monolayer Cu_3BHT the same photoexcitation evokes no discernible $\Delta\sigma$. This is because the intrinsic charge carrier mobility of Cu_3BHT is much lower than that of graphene. Notably, the vdWh manifests negative $\Delta\sigma$ dynamics featuring a rapid decay process within the first few ps, followed by a much slower decay spanning tens of ps. The rapid decay

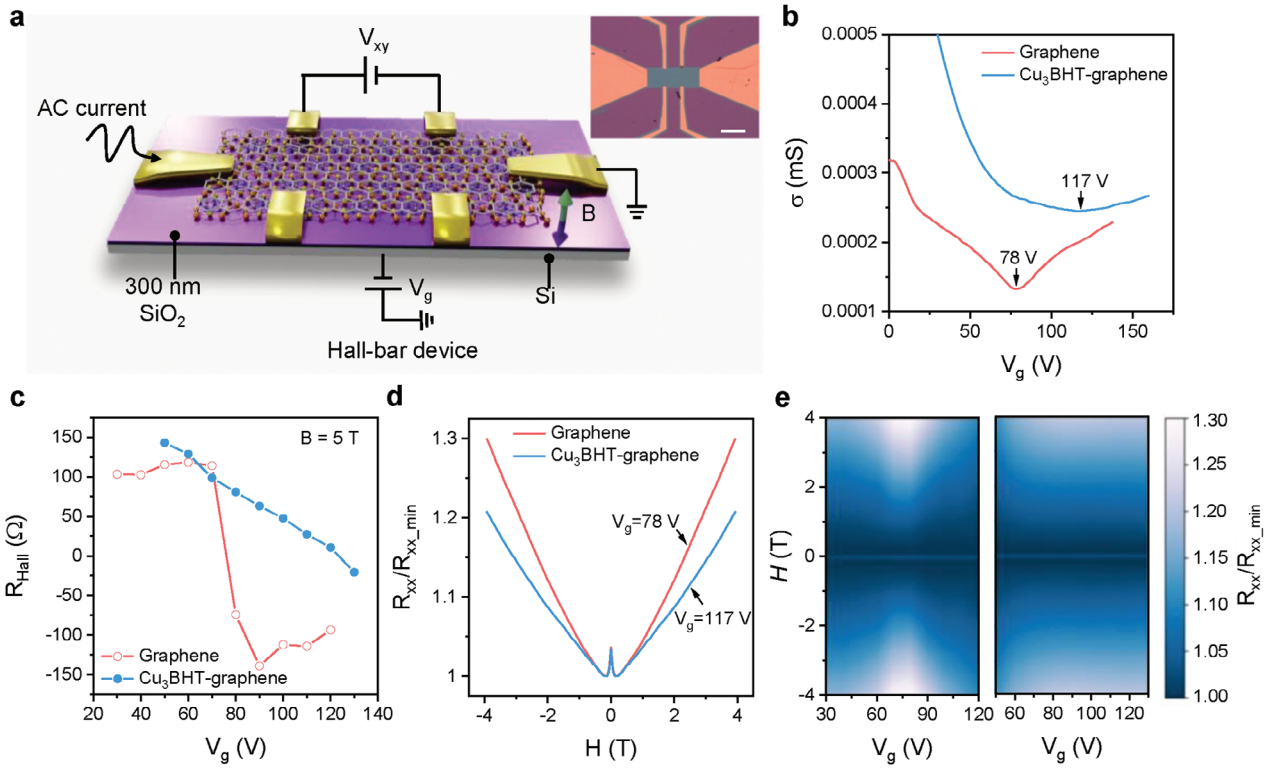

Figure 3. Electrical study of CT in Cu_3BHT-graphene vdWh. a) Schematic illustration of the gated Hall bar device. Inset: Optical image of the gated Hall bar device. Scale bar, 50 μm. b) Gate-voltage-dependent longitudinal conductance of pristine graphene and Cu_3BHT-graphene vdWh at 2 K, respectively. As the gate voltage increases, the E_F in graphene passes through the Dirac point, leading to a transition in the type of graphene from hole accumulation to electron accumulation. The conductance in graphene initially decreases as the E_F approaches the Dirac point, followed by an increase when E_F departs from the Dirac point. c) Gate-voltage-dependent Hall resistance of pristine graphene and Cu_3BHT-graphene vdWh under 5 T magnetic field, respectively. d) Normalized longitudinal resistances R_{xx}/R_{xx_min} of graphene and Cu_3BHT-graphene vdWh versus field, with applied gate voltage 78 and 117 V, respectively. A broadened valley manifests that the incorporation of Cu_3BHT indeed impacts the band structure of graphene. e) Mapping of pristine graphene and Cu_3BHT-graphene vdWh's normalized longitudinal resistances R_{xx}/R_{xx_min}, measured with varied magnetic fields and different gate voltages.

process can be attributed to hot carrier relaxation in graphene, while the subsequent relatively slow decay process can be rationalized by interlayer charge recombination following ultrafast photoinduced CT.[25,26,27] Specifically, upon photoexcitation, charge carriers are initially injected into both layers. Subsequently, ultrafast photoinduced CT occurs at the interface between monolayer Cu_3BHT and graphene, modulating the carrier density (and thus $\Delta\sigma$) in the graphene layer. As the graphene layer in the vdWh is initially p-doped, the negative sign of the CT-induced $\Delta\sigma$ in tens of ps provides direct evidence for the photon-induced electron flow from monolayer Cu_3BHT to graphene (Figure 4c). This is followed by interlayer recombination involving electrons residing in graphene and holes residing in monolayer Cu_3BHT. A single exponential fit to the relatively slow decay process yields an interlayer recombination lifetime of ≈56 ps. The reason for the observed photoinduced net electron (rather than hole) transfer from Cu_3BHT to graphene and the relatively long-lived holes remaining in Cu_3BHT can be tentatively attributed to the static built-in electric field directed from graphene toward Cu_3BHT.[28] This facilitates the transfer of photogenerated electrons from Cu_3BHT to graphene while hindering the transfer of photogenerated holes from Cu_3BHT to graphene.

To quantitatively characterize the photoinduced interlayer charge separation process, we measured the CT-induced frequency-resolved complex photoconductivity $\Delta\sigma(\omega)$. The measurements were performed at a pump-probe delay of ≈50 ps to eliminate the influence of hot carriers in graphene, allowing the determination of CT-induced changes in the charge transport properties (i.e., carrier density and charge scattering time) from $\Delta\sigma(\omega)$. As shown in Figure 4d, $\Delta\sigma(\omega)$ obtained at different pump fluences can be well described by the conductivity difference between two quasi-equilibrium states in graphene (i.e., before and after CT, Equation (2))

$$\Delta\sigma(\omega) = \sigma'(\omega) - \sigma(\omega) = \frac{D'}{\pi}\frac{1}{\left(\frac{1}{\tau'} - i\omega\right)} - \frac{D}{\pi}\frac{1}{\left(\frac{1}{\tau} - i\omega\right)} \quad (2)$$

where D and τ are the initial Drude weight and charge scattering time before CT (obtained from the Drude fit shown in Figure 2e), and D' and τ' are the Drude weight and carrier scattering time after CT (at a pump-probe delay of ≈50 ps). The fitting reveals that the change in carrier density dominates the CT-induced $\Delta\sigma(\omega)$ while the carrier scattering time remains almost constant. As shown in Figure 4e, the linear relationship

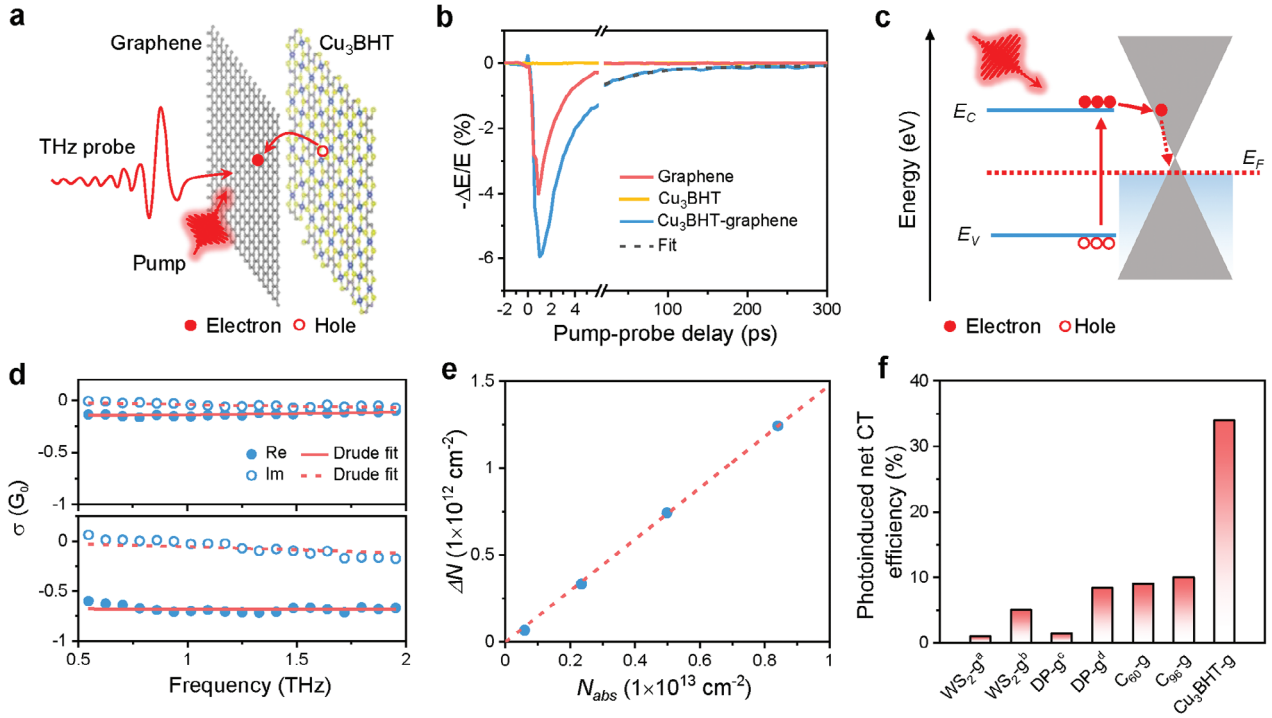

Figure 4. Efficient photoinduced CT at the Cu_3BHT-graphene interface. a) Schematic of TRTS. b) THz $\Delta\sigma$ dynamics of bare graphene, Cu_3BHT, and Cu_3BHT-graphene vdWh following photoexcitation (1.55 eV, 28 μJ cm^{-2}). The measurements were performed in a dry N_2-purged environment. c) Schematic of band alignment of Cu_3BHT-graphene vdWh and photoinduced electron transfer process from Cu_3BHT to graphene. d) Frequency-resolved complex photoconductivity $\Delta\sigma(\omega)$ for Cu_3BHT-graphene vdWh at a pump-probe delay of ≈50 ps following photoexcitation (the incident pump fluences are 2.3 (top) and 32.6 μJ cm^{-2} (bottom), respectively). The solid and dashed lines are the fits to the real and imaginary components of $\Delta\sigma(\omega)$, following the differential Drude model describing the conductivity difference between two quasi-equilibrium states. e) Quantification of photoinduced electron transfer efficiency in Cu_3BHT-graphene vdWh. f) Comparison of photoinduced net CT efficiencies characterized by THz spectroscopy. Note that we restricted the comparison to the same technique to eliminate differences arising from different evaluation protocols. Photoinduced net CT efficiencies for WS_2-graphene vdWhs (WS_2-g) are obtained under [a]1.55 eV and [b]3.10 eV excitations;[29] photoinduced net CT efficiencies for double perovskite-graphene vdWhs (DP-g) are obtained under [c]3.10 eV and [d]2 eV excitations;[25] photoinduced net CT efficiencies for $C_{60}H_{22}$-graphene vdWhs (C_{60}-g) and $C_{96}H_{24}$-graphene vdWhs (C_{96}-g) are obtained under 3.10 eV excitation.[9,26]

between the CT-induced carrier density changes in graphene (N_{CT}) and the absorbed photon density in Cu_3BHT (N_{abs}) indicates that the photon-induced net electron transfer efficiency (η), that is, the difference between the photon-induced electron transfer efficiency and the hole transfer efficiency from Cu_3BHT to graphene, is ≈15% over the used pump fluence range. Note that the estimated η represents the lower limit of electron transfer efficiency, partly because partial back recombination occurs within 50 ps. By extrapolating the $\Delta\sigma$ or η to the photoconductivity at 10 ps (where the photoresponse of bare graphene is approximately null), we estimate η up to 34%. Furthermore, the photon-to-charge conversion ratio is over-assumed to be 100% (resulting in underestimation of η). Nevertheless, the estimated η is substantially higher than that of reported inorganic vdWhs such as C_{60}-graphene, nanographene-graphene, and WS_2-graphene vdWhs characterized by the same method (typically less than 10%) (Figure 4f).[9,29,26] Note that the broadband absorption of Cu_3BHT, effective net electron transfer from Cu_3BHT to graphene, and relatively long interlayer charge separation time facilitate conductance modulation through the photogating effect,[30] making Cu_3BHT-graphene vdWHs promising candidates for designing broadband photodetectors with ultrahigh photoconductive gain and responsivity.[26,28]

3. Conclusion

In conclusion, we have fabricated a new type of 2D vdWh consisting of π-d conjugated Cu_3BHT and graphene, characterized by intimate interfacial contact. Monolayer Cu_3BHT with a planar structure was synthesized on the water surface, forming a polycrystalline and large-area film with an atomically flat surface. Using imaging and diffraction techniques, the atomic structure of monolayer Cu_3BHT was determined in real space with a resolution of ≈1.2 Å. Optical and electrical studies, as well as theoretical calculations, unveil the strong interlayer coupling between Cu_3BHT and graphene, leading to highly efficient photoinduced interlayer charge separation with a net electron transfer efficiency of ≈34% from Cu_3BHT to graphene, which sets a new record and far exceeds those reported for bilayer 2D vdWhs and molecular-graphene vdWhs. Our findings lay the foundation for the creation of novel vdWhs with modulated band alignment and interlayer orbital coupling by integrating monolayer 2DCPs or 2D c-MOFs (e.g., FeTHT, THT = 2,3,6,7,10,11-triphenylenehexathiol) with inorganic 2D crystals (e.g., graphene, TMDs, and h-BN), and will propel the exploitation of intriguing physical phenomena and specific optoelectronic devices.

4. Experimental Section

Synthesis of Monolayer Cu_3BHT: The monolayer Cu_3BHT was synthesized on the water surface of a Langmuir–Blodgett through (KSV NIMA), which was equipped with a platinum Wilhelmy plate, a Taflon dipper, and a pair of Delrin barriers. During the synthesis, 50 µL of BHT solution (0.3 mg mL^{-1}) in chloroform/dimethylformamide (2:1, v/v) was spread on the water surface with a microsyringe. The solvent was allowed to evaporate for 30 min and then the compression was carried out by the barriers at a rate of 2 mm min^{-1} until the surface pressure reached 10 mN m^{-1}. Then, 5 mL $Cu(NO_3)_2$ aqueous solution (1 mg mL^{-1}) was injected into the water subphase to initiate the coordination polymerization. After 5 h, the synthetic monolayer Cu_3BHT film was deposited onto the substrates by the horizontal dipping method. The samples were immersed in Milli-Q water for 5 min, rinsed with flowing ethanol and acetone, and then dried at 80 °C.

Fabrication of Cu_3BHT-Graphene vdWh: The monolayer Cu_3BHT films on the water surface were first transferred onto the substrate (e.g., SiO_2 (300 nm)/Si, quartz). The transfer of CVD graphene purchased from Graphenea started from an etching of backside graphene via O_2 plasma and the removal of copper foil with the ammonium persulfate (APS) copper etchant.[31] Then, the PMMA (thickness, 60 nm)-coated graphene film was transferred to a Milli-Q water surface to wash off the remaining etchant, followed by deposition of it onto the target monolayer Cu_3BHT-coated substrate. Finally, the PMMA was removed with acetone and annealed at 300 °C under an H_2-Ar atmosphere, resulting in Cu_3BHT-graphene vdWhs.

Raman Spectroscopy: Raman spectra and mappings were collected using a 532 nm laser excitation with a beam size of ≈1 µm (Witec alpha300 R confocal Raman imaging microscopes, Germany). The strain and doping effects in graphene after exposure to Cu_3BHT were deconvoluted from the G-band and 2D-band frequency correlation according to the previous report.[13b]

Computational Details: All structures were optimized using FHI-aims[32] with PBE[33] functional and tight tier 1 basis,[32a] and Tkatchenko–Scheffler dispersion correction.[34] Γ-centered k-grids of 12 × 12 × 1, 24 × 24 × 1, and 24 × 12 × 1 for Cu_3BHT-graphene (3°), Cu_3BHT-graphene (12°), and Cu_3BHT-graphene (29°), respectively, were used for both optimization and electronic properties calculations. A correction to compensate for a potential surface dipole was used for electronic properties calculations, as implemented in FHI-aims.

Time-Resolved Terahertz Spectroscopy: A regenerative amplified and mode-locked titanium-sapphire system was employed to deliver ultrashort laser pulses with a central wavelength of 1.55 eV, a pulse duration of ≈50 fs, and a repetition rate of 1 kHz. The produced laser pulses were then split to enable optical excitation, THz generation (via optical rectification), and THz detection (via free-space electro-optic sampling). The optical injection of charge carriers in the Cu_3BHT-graphene vdWh was triggered by the fundamental 1. 55 eV ultrashort pulsed laser. The resulting $\Delta\sigma$ was then interrogated by a freely propagating single-cycle THz pulse (≈1 ps duration) and recorded as a function of time: $\Delta\sigma$ was linearly proportional to the pump-induced attenuation in the THz electric field ($-\Delta E/E$).[23] The measurements were performed in a dry N_2-purged environment to minimize THz absorption of water vapor. The frequency-resolved sheet conductivity was obtained by measuring time-dependent THz waveforms transmitted through the target and reference regions, performing an FFT, and applying the thin-film approximation (Equation (3))[35]

$$\sigma(\omega) = \frac{n+1}{Z_0}\left(\frac{E_0(\omega)}{E(\omega)} - 1\right) \tag{3}$$

where $E_0(\omega)$ is the frequency-dependent THz field through the reference region, $E(\omega)$ is the frequency-dependent THz field through the target region, $Z_0 = 377\ \Omega$ is the impedance of free space, and n is the refractive index of the substrate in the THz range (here $n = 1.95$ was used for the fused silica substrate). As discussed in the main text, the obtained $\sigma(\omega)$ can be described by the Drude model. The carrier density (N) and the absolute value of the Fermi level ($|E_F|$) in graphene can be calculated from the obtained Drude weight by Equations (4) and (5), respectively

$$D = \frac{\nu_F e^2}{\hbar}\sqrt{\pi N} \tag{4}$$

$$|E_F| = \hbar\nu_F(\pi|N|)^{1/2} \tag{5}$$

Frequency-dependent sheet photoconductivity (ω) can be obtained by processing Equation (3) in the small differential limit, as shown in Equation (6)

$$\Delta\sigma(\omega) = -\frac{n+1}{Z_0}\left(\frac{E_{pump}(\omega) - E(\omega)}{E(\omega)}\right) \tag{6}$$

where $E_{pump}(\omega)$ and $E(\omega)$ are frequency-dependent THz electrical fields transmitted through the sample with and without photoexcitation, respectively.

Supporting Information

Supporting Information is available from the Wiley Online Library or from the author.

Acknowledgements

Z.W., S.F., and W.Z. contributed equally to this work. This work was financially supported by the National Natural Science Foundation of China (22272092), ERC starting grant (FC2DMOF, No. 852909), ERC Consolidator Grant (T2DCP), DFG project (2D polyanilines, No. 426572620), H2020-FETOPEN (PROGENY, 899205), CRC 1415 (Chemistry of Synthetic Two-Dimensional Materials, No. 417590517), SPP 2244 (2DMP), GRK2861 (No. 491865171), EMPIR-20FUN03-COMET, as well as the German Science Council and Center of Advancing Electronics Dresden (cfaed). R.D. thanks Taishan Scholars Program of Shandong Province (tsqn201909047) and the Natural Science Foundation of Shandong Province (ZR2023JQ005). The authors acknowledge cfaed and Dresden Center for Nanoanalysis (DCN) at TUD and Dr. Petr Formanek, Prof. Andreas Fery, Anna Maria Dominic, and Prof. Inez M. Weidinger for the use of the TEM facility at IPF, as well as the Raman measurement. The authors acknowledge SOLEIL for the provision of synchrotron radiation facilities and the authors would like to thank Dr. Arnaud Hemmerle for assistance in using beamline SIRIUS. T.L., M.P., and T.H. thank ZIH Dresden for the use of computational resources.

Open access funding enabled and organized by Projekt DEAL.

Conflict of Interest

The authors declare no conflict of interest.

Data Availability Statement

The data that support the findings of this study are available from the corresponding author upon reasonable request.

Keywords

conductive 2D coordination polymers, 2D van der Waals heterostructures, interlayer coupling, charge separation

Received: October 31, 2023
Revised: February 9, 2024
Published online: March 3, 2024

[1] a) B. Hunt, J. D. Sanchez-Yamagishi, A. F. Young, M. Yankowitz, B. J. LeRoy, K. Watanabe, T. Taniguchi, P. Moon, M. Koshino, P. Jarillo-Herrero, *Science* **2013**, *340*, 1427; b) M. Yankowitz, Q. Ma, P. Jarillo-Herrero, B. J. LeRoy, *Nat. Rev. Phys.* **2019**, *1*, 112; c) K. S. Novoselov, A. Mishchenko, A. Carvalho, A. H. Castro Neto, *Science* **2016**, *353*, aac9439.

[2] Y. Liu, N. O. Weiss, X. Duan, H.-C. Cheng, Y. Huang, X. Duan, *Nat. Rev. Mater.* **2016**, *1*, 16042.

[3] C. Jin, E. Y. Ma, O. Karni, E. C. Regan, F. Wang, T. F. Heinz, *Nat. Nanotechnol.* **2018**, *13*, 994.

[4] T. Georgiou, R. Jalil, B. D. Belle, L. Britnell, R. V. Gorbachev, S. V. Morozov, Y.-J. Kim, A. Gholinia, S. J. Haigh, O. Makarovsky, L. Eaves, L. A. Ponomarenko, A. K. Geim, K. S. Novoselov, A. Mishchenko, *Nat. Nanotechnol.* **2013**, *8*, 100.

[5] a) X. Zhou, X. Hu, S. Zhou, H. Song, Q. Zhang, L. Pi, L. Li, H. Li, J. Lü, T. Zhai, *Adv. Mater.* **2018**, *30*, 1703286; b) Y. Chen, C. Tan, Z. Wang, J. Miao, X. Ge, T. Zhao, K. Liao, H. Ge, Y. Wang, F. Wang, Y. Zhou, P. Wang, X. Zhou, C. Shan, H. Peng, W. Hu, *Sci. Adv.* **2022**, *8*, eabq1781; c) H. Jiao, X. Wang, Y. Chen, S. Guo, S. Wu, C. Song, S. Huang, X. Huang, X. Tai, T. Lin, H. Shen, H. Yan, W. Hu, X. Meng, J. Chu, Y. Zhang, J. Wang, *Sci. Adv.* **2022**, *8*, eabn1811.

[6] F. Withers, O. Del Pozo-Zamudio, A. Mishchenko, A. P. Rooney, A. Gholinia, K. Watanabe, T. Taniguchi, S. J. Haigh, A. K. Geim, A. I. Tartakovskii, K. S. Novoselov, *Nat. Mater.* **2015**, *14*, 301.

[7] a) Y. Zhong, B. Cheng, C. Park, A. Ray, S. Brown, F. Mujid, J.-U. Lee, H. Zhou, J. Suh, K.-H. Lee, *Science* **2019**, *366*, 1379; b) K. Liu, J. Li, H. Qi, M. Hambsch, J. Rawle, A. R. Vázquez, A. S. Nia, A. Pashkin, H. Schneider, M. Polozij, T. Heine, M. Helm, S. C. B. Mannsfeld, U. Kaiser, R. Dong, X. Feng, *Angew. Chem., Int. Ed.* **2021**, *60*, 13859; c) R. Dong, M. Pfeffermann, H. Liang, Z. Zheng, X. Zhu, J. Zhang, X. Feng, *Angew. Chem., Int. Ed.* **2015**, *54*, 12058.

[8] H. Sahabudeen, H. Qi, B. A. Glatz, D. Tranca, R. Dong, Y. Hou, T. Zhang, C. Kuttner, T. Lehnert, G. Seifert, U. Kaiser, A. Fery, Z. Zheng, X. Feng, *Nat. Commun.* **2016**, *7*, 13461.

[9] X. Yu, S. Fu, M. Mandal, X. Yao, Z. Liu, W. Zheng, P. Samorì, A. Narita, K. Müllen, D. Andrienko, M. Bonn, H. I. Wang, *J. Chem. Phys.* **2022**, *156*, 074702.

[10] H. Sahabudeen, H. Qi, B. A. Glatz, D. Tranca, R. Dong, Y. Hou, T. Zhang, C. Kuttner, T. Lehnert, G. Seifert, *Nat. Commun.* **2016**, *7*, 13461.

[11] a) X. Huang, P. Sheng, Z. Tu, F. Zhang, J. Wang, H. Geng, Y. Zou, C. Di, Y. Yi, Y. Sun, W. Xu, D. Zhu, *Nat. Commun.* **2015**, *6*, 7408; b) X. Huang, S. Zhang, L. Liu, L. Yu, G. Chen, W. Xu, D. Zhu, *Angew. Chem., Int. Ed.* **2018**, *130*, 152.

[12] a) M. Van Wijk, A. Schuring, M. Katsnelson, A. Fasolino, *Phys. Rev. Lett.* **2014**, *113*, 135504; b) J. Li, X. Yang, Y. Liu, B. Huang, R. Wu, Z. Zhang, B. Zhao, H. Ma, W. Dang, Z. Wei, K. Wang, Z. Lin, X. Yan, M. Sun, B. Li, X. Pan, J. Luo, G. Zhang, Y. Liu, Y. Huang, X. Duan, X. Duan, *Nature* **2020**, *579*, 368; c) S. S. Sunku, G. X. Ni, B. Y. Jiang, H. Yoo, A. Sternbach, A. S. McLeod, T. Stauber, L. Xiong, T. Taniguchi, K. Watanabe, P. Kim, M. M. Fogler, D. N. Basov, *Science* **2018**, *362*, 1153; d) L. J. McGilly, A. Kerelsky, N. R. Finney, K. Shapovalov, E.-M. Shih, A. Ghiotto, Y. Zeng, S. L. Moore, W. Wu, Y. Bai, K. Watanabe, T. Taniguchi, M. Stengel, L. Zhou, J. Hone, X. Zhu, D. N. Basov, C. Dean, C. E. Dreyer, A. N. Pasupathy, *Nat. Nanotechnol.* **2020**, *15*, 580.

[13] a) A. Das, S. Pisana, B. Chakraborty, S. Piscanec, S. K. Saha, U. V. Waghmare, K. S. Novoselov, H. R. Krishnamurthy, A. K. Geim, A. C. Ferrari, A. K. Sood, *Nat. Nanotechnol.* **2008**, *3*, 210; b) J. E. Lee, G. Ahn, J. Shim, Y. S. Lee, S. Ryu, *Nat. Commun.* **2012**, *3*, 1024.

[14] a) P. Drude, *Ann. Phys.* **1900**, *308*, 369; b) P. Drude, *Ann. Phys.* **1900**, *306*, 566.

[15] M.-H. Chiu, M.-Y. Li, W. Zhang, W.-T. Hsu, W.-H. Chang, M. Terrones, H. Terrones, L.-J. Li, *ACS Nano* **2014**, *8*, 9649.

[16] X. Zhang, Y. Zhou, B. Cui, M. Zhao, F. Liu, *Nano Lett.* **2017**, *17*, 6166.

[17] a) H. Fang, C. Battaglia, C. Carraro, S. Nemsak, B. Ozdol, J. S. Kang, H. A. Bechtel, S. B. Desai, F. Kronast, A. A. Unal, G. Conti, C. Conlon, G. K. Palsson, M. C. Martin, A. M. Minor, C. S. Fadley, E. Yablonovitch, R. Maboudian, A. Javey, *Proc. Natl. Acad. Sci. U. S. A.* **2014**, *111*, 6198; b) K. Liu, L. Zhang, T. Cao, C. Jin, D. Qiu, Q. Zhou, A. Zettl, P. Yang, S. G. Louie, F. Wang, *Nat. Commun.* **2014**, *5*, 4966.

[18] a) Y. Shi, X. Dong, P. Chen, J. Wang, L.-J. Li, *Phys. Rev. B* **2009**, *79*, 115402; b) R. A. Nistor, M. A. Kuroda, A. A. Maarouf, G. J. Martyna, *Phys. Rev. B* **2012**, *86*, 041409.

[19] Y. Yang, R. Murali, *Appl. Phys. Lett.* **2011**, *98*, 093116.

[20] J. Shin, G. A. Gamage, Z. Ding, K. Chen, F. Tian, X. Qian, J. Zhou, H. Lee, J. Zhou, L. Shi, T. Nguyen, F. Han, M. Li, D. Broido, A. Schmidt, Z. Ren, G. Chen, *Science* **2022**, *377*, 437.

[21] E. McCann, K. Kechedzhi, V. I. Fal'ko, H. Suzuura, T. Ando, B. L. Altshuler, *Phys. Rev. Lett.* **2006**, *97*, 146805.

[22] S. Cho, M. S. Fuhrer, *Phys. Rev. B* **2008**, *77*, 081402.

[23] R. Ulbricht, E. Hendry, J. Shan, T. F. Heinz, M. Bonn, *Rev. Mod. Phys.* **2011**, *83*, 543.

[24] a) S. F. Shi, T. T. Tang, B. Zeng, L. Ju, Q. Zhou, A. Zettl, F. Wang, *Nano Lett.* **2014**, *14*, 1578; b) A. J. Frenzel, C. H. Lui, Y. C. Shin, J. Kong, N. Gedik, *Phys. Rev. Lett.* **2014**, *113*, 056602; c) G. Jnawali, Y. Rao, H. Yan, T. F. Heinz, *Nano Lett.* **2013**, *13*, 524.

[25] H. Zhang, E. Debroye, S. Fu, M. C. R. González, I. du Fossé, J. J. Geuchies, L. Gao, X. Yu, A. J. Houtepen, S. De Feyter, J. Hofkens, M. Bonn, H. I. Wang, *Adv. Mater.* **2023**, *35*, 2211198.

[26] Z. Liu, H. Qiu, S. Fu, C. Wang, X. Yao, A. G. Dixon, S. Campidelli, E. Pavlica, G. Bratina, S. Zhao, L. Rondin, J.-S. Lauret, A. Narita, M. Bonn, K. Müllen, A. Ciesielski, H. I. Wang, P. Samorì, *J. Am. Chem. Soc.* **2021**, *143*, 17109.

[27] S. Fu, X. Jia, A. S. Hassan, H. Zhang, W. Zheng, L. Gao, L. Di Virgilio, S. Krasel, D. Beljonne, K.-J. Tielrooij, M. Bonn, H. I. Wang, *Nano Lett.* **2023**, *23*, 1850.

[28] a) G. Konstantatos, M. Badioli, L. Gaudreau, J. Osmond, M. Bernechea, F. P. G. de Arquer, F. Gatti, F. H. L. Koppens, *Nat. Nanotechnol.* **2012**, *7*, 363; b) Y. Xiong, Q. Liao, Z. Huang, X. Huang, C. Ke, H. Zhu, C. Dong, H. Wang, K. Xi, P. Zhan, F. Xu, Y. Lu, *Adv. Mater.* **2020**, *32*, 1907242.

[29] S. Fu, I. du Fossé, X. Jia, J. Xu, X. Yu, H. Zhang, W. Zheng, S. Krasel, Z. Chen, Z. M. Wang, K.-J. Tielrooij, M. Bonn, A. J. Houtepen, H. I. Wang, *Sci. Adv.* **2021**, *7*, eabd9061.

[30] a) H. Fang, W. Hu, *Adv. Sci.* **2017**, *4*, 1700323; b) F. H. L. Koppens, T. Mueller, P. Avouris, A. C. Ferrari, M. S. Vitiello, M. Polini, *Nat. Nanotechnol.* **2014**, *9*, 780.

[31] a) F. Kafiah, Z. Khan, A. Ibrahim, M. Atieh, T. Laoui, *Materials* **2017**, *10*, 86; b) W. Regan, N. Alem, B. Alemán, B. Geng, Ç. Girit, L. Maserati, F. Wang, M. Crommie, A. Zettl, *Appl. Phys. Lett.* **2010**, *96*, 113102.

[32] a) V. Blum, R. Gehrke, F. Hanke, P. Havu, V. Havu, X. Ren, K. Reuter, M. Scheffler, *Comput. Phys. Commun.* **2009**, *180*, 2175; b) X. Ren, P. Rinke, V. Blum, J. Wieferink, A. Tkatchenko, A. Sanfilippo, K. Reuter, M. Scheffler, *New J. Phys.* **2012**, *14*, 053020.

[33] J. P. Perdew, K. Burke, M. Ernzerhof, *Phys. Rev. Lett.* **1996**, *77*, 3865.

[34] A. Tkatchenko, M. Scheffler, *Phys. Rev. Lett.* **2009**, *102*, 073005.

[35] J. Neu, K. P. Regan, J. R. Swierk, C. A. Schmuttenmaer, *Appl. Phys. Lett.* **2018**, *113*, 233901.